

Simulating Silicon Photomultiplier Response to Scintillation Light

Abhinav K. Jha, Herman T. van Dam, Matthew A. Kupinski, and Eric Clarkson

Abstract—The response of a Silicon Photomultiplier (SiPM) to optical signals is affected by many factors including photon-detection efficiency, recovery time, gain, optical crosstalk, afterpulsing, dark count, and detector dead time. Many of these parameters vary with overvoltage and temperature. When used to detect scintillation light, there is a complicated non-linear relationship between the incident light and the response of the SiPM. In this paper, we propose a combined discrete-time discrete-event Monte Carlo (MC) model to simulate SiPM response to scintillation light pulses. Our MC model accounts for all relevant aspects of the SiPM response, some of which were not accounted for in the previous models. We also derive and validate analytic expressions for the single-photoelectron response of the SiPM and the voltage drop across the quenching resistance in the SiPM microcell. These analytic expressions consider the effect of all the circuit elements in the SiPM and accurately simulate the time-variation in overvoltage across the microcells of the SiPM. Consequently, our MC model is able to incorporate the variation of the different SiPM parameters with varying overvoltage. The MC model is compared with measurements on SiPM-based scintillation detectors and with some cases for which the response is known *a priori*. The model is also used to study the variation in SiPM behavior with SiPM-circuit parameter variations and to predict the response of a SiPM-based detector to various scintillators.

Index Terms—Circuit transient analysis, electrical characteristics, Monte Carlo model, silicon photomultiplier, single-photoelectron response.

I. INTRODUCTION

SILICON photomultipliers (SiPMs) are emerging as photon-sensing devices in many applications due to their attractive features such as low operating voltage, small size, extremely high gain, immunity to magnetic fields, fast turn-on and turn-off times, stability, compactness, and robustness [1]–[9]. They are being studied for use in many applications to detect scintillation light, such as in positron emission tomography (PET) systems [10]–[15], multimodality PET-magnetic

resonance imaging (MRI) systems [16], [17], single photon emission computed tomography (SPECT) systems [18], and high-energy physics systems [19], [20], [21], [22]. Due to this wide usage, many tasks have emerged that require relating the SiPM output to scintillation light. These tasks include optimizing the design of the SiPM-based detector for a particular application, estimating difficult-to-measure SiPM parameters, determining event time for time-of-flight (TOF) PET systems, determining the location of interaction of a gamma-ray photon with the scintillation crystal in a nuclear imaging system, performing corrections on measurements of energy spectra, studying statistics of scintillation light, predicting scintillation-detector performance such as energy resolution, evaluating imaging systems that use SiPMs, and calibrating SiPM-based detectors [20], [23]–[25]. However, the relationship between SiPM output and scintillation light is complex. The performance of a SiPM-based detector is significantly affected by the inherent non-proportionality of the SiPM response. SiPMs suffer from non-linear effects, parameter variation due to varying overvoltage, and noise phenomena such as optical crosstalk, afterpulsing, and dark counts [26]. Scintillation light pulses are inhomogeneous-intensity processes and can have a long decay time and/or high light yield. As a result, the behavior of the SiPM varies within the duration of the scintillation pulse, further complicating this relationship [25]. To deal with this complexity, we require models that relate the measured electronic signal with the input optical signal.

There has been research to model SiPM response using both analytical and Monte Carlo (MC) simulation approaches. Van Dam *et al.* [24] have developed a completely analytical model that simulates SiPM response based on the physical and functional principles that are generally applicable to scintillation light pulses. Although analytical models are useful, it is difficult for these models to account for all processes that occur in the SiPM, such as variation of SiPM parameters with overvoltage, effect of output voltage, deadtime, and dark counts. Moreover, it is complicated to obtain an accurate analytic expression for the variance of the SiPM output. Computation of the output variance is useful in many tasks such as determining the energy resolution of detectors or determining the interaction-location of a gamma-ray photon using maximum-likelihood methods in a nuclear-imaging system [27]. Due to these reasons, MC simulation approaches are an important alternative method. The MC model can account for all the relevant SiPM phenomena, and be used to obtain accurate SiPM response and variance of the SiPM output.

A SiPM consists of an array of Geiger-mode avalanche photodiodes (GM-APDs), also known as microcells [24]. Circuit-

Manuscript received April 20, 2012; revised August 31, 2012 and November 17, 2012; accepted November 23, 2012. Date of publication January 30, 2013; date of current version February 06, 2013. This work was supported by the National Institute of Biomedical Imaging and Bioengineering of National Institute of Health under Grants RC1-EB010974, R37-EB000803, and P41-EB002035. A. K. Jha was supported in part by the Technology Research Initiative Fund (TRIF) Imaging Fellowship.

A. K. Jha is with the College of Optical Sciences, University of Arizona, Tucson AZ 85721 USA.

H. T. van Dam is with the Department of Radiation, Detection and Medical Imaging, Delft University of Technology, Delft, 2629 JB, The Netherlands.

M. A. Kupinski and E. Clarkson are with the College of Optical Sciences and the Department of Medical Imaging, University of Arizona, Tucson AZ 85721 USA.

Color versions of one or more of the figures in this paper are available online at <http://ieeexplore.ieee.org>.

Digital Object Identifier 10.1109/TNS.2012.2234135

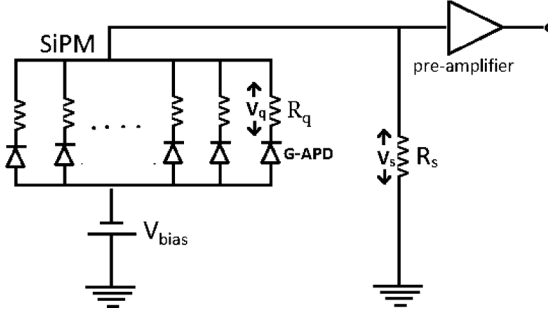


Fig. 1. Schematic of a SiPM and its readout circuit.

simulation studies have examined the electronic response of an individual microcell [28], [29]. These studies have been extended for SiPMs [30], [31], but they primarily address sources that emit fast light pulses, e.g., light emitted from a fast laser source. Thus, these studies do not consider many effects that arise when the light pulse is of a similar duration as the SiPM recovery time. To simulate the SiPM output to constant-intensity light, MC models have been developed [32], but these models do not consider the variation in light intensity and device response with time, as is required for modeling SiPM response to scintillation light. MC models to simulate SiPM response to scintillation light have also been designed [21], [25], [33]–[35]. However, most of these models focus on simulating some specific aspects of the SiPM response, or specific input scintillation-light characteristics. Thus, they do not model all the relevant SiPM phenomena. Moreover, in these models, the effect of the different SiPM-circuit elements on the single-photoelectron response and the voltage drop across the SiPM microcell is not explicitly considered. Therefore, the electrical characteristics of the SiPM are not modeled accurately.

A simulation of SiPM response to scintillation light that includes all relevant processes should satisfy many criteria, such as SiPM-state change on occurrence of an avalanche, stochastic nature of afterpulsing, optical crosstalk, and dark count processes, voltage drop across the readout circuit, and the variation in the different SiPM parameters, namely the gain, internal quantum efficiency (QE), dark count rate, optical crosstalk and afterpulsing probability, within the duration of the scintillation pulse. The model should also account for the electrical characteristics of the SiPM circuit and accurately simulate the transient response of the output due to an avalanche. This is required to accurately determine the probability of a photon triggering an avalanche and the magnitude of output charge due to such an avalanche. Finally, the dependence of the various SiPM parameters on temperature, and phenomena such as the dead time of microcells following an avalanche should be considered.

Considering the above-mentioned criteria, to simulate the SiPM response in a computationally efficient manner, we treat the problem as a combined discrete-time discrete-event process [36], [37]. We first develop techniques to accurately model SiPM electrical response, optical crosstalk, afterpulsing, effects due to the readout circuit, variation in SiPM parameters within the duration of the scintillation pulse, and the dead time. We also derive a novel analytic expression for the single-photoelectron response and voltage drop across the SiPM circuit elements

when an avalanche occurs. These expressions account for the effect of all the circuit elements in the SiPM at any instant of time and thus help us accurately simulate SiPM-parameter variation. The simulation mechanism then integrates all these methods using the discrete-time discrete-event framework. Thus, the software simulates SiPM phenomena that were not completely considered in the previous models.

In the sections to follow, we elaborate further on the simulation. We first discuss the various phenomena that contribute to the SiPM response to a scintillation light pulse and, in the process, derive the expression for the single-photoelectron response of the SiPM.

II. SiPM RESPONSE TO SCINTILLATION LIGHT PULSE

A. SiPM Circuit Response

Consider a gamma-ray photon with energy E that interacts within a scintillator, with light yield Y (expressed in optical photons per unit deposited energy), and deposits its energy at the interaction point. Consequently a scintillation pulse is produced, which is typically an inhomogeneous intensity Poisson process [38]. A fraction f of the scintillation photons is absorbed in the active volume of the SiPM, where f denotes the photon-collection efficiency of the SiPM.

A schematic of the SiPM and its readout circuit are shown in Fig. 1. A SiPM is composed of about $10^2 - 10^5$ microcells, each of which are reverse biased at voltage V_{bias} and in series with a quenching resistor R_q . Each microcell is biased above the breakdown voltage by an amount V_{ob} , also referred to as overvoltage. When no current is flowing across the SiPM, the initial overvoltage, which we denote by V_{ob0} is

$$V_{ob0} = V_{bias} - V_{br} \quad (1)$$

where V_{br} is the breakdown voltage of the microcell. However, when current flow occurs through the SiPM, V_{ob} across the microcell decreases due to the voltage drop across the quenching resistance and the readout-circuit resistance.

When a photon is incident on one of the microcells of the SiPM, it might create an electron-hole pair in the microcell, which might then trigger an avalanche. The process of creating an electron-hole pair and triggering an avalanche have a joint probability ϵ , which is defined as the internal QE of a single microcell [24]. The probability of triggering an avalanche varies with overvoltage V_{ob} [21], [26], [39]. The SiPM detector photon-detection efficiency (PDE) is defined as the product of the internal QE ϵ and the photon-collection efficiency f .

The triggering of the avalanche results in microplasma current, which rises swiftly with nanosecond or sub-nanosecond rise time τ_{mr} to a value in the milliamperage range [25], [40], [41]. This leads to current flow in the circuit, which causes a voltage drop V_q across the quenching resistance R_q as shown in Fig. 1. Due to this voltage drop, the voltage and microplasma current across the GM-APD reduce exponentially to their steady-state values, with a decay time τ_{md} . As the voltage across the diode reduces to V_{br} , the intensity of the microplasma current becomes very low, the number of carriers that traverse the avalanche region becomes very small, and eventually the avalanche is quenched. Therefore, this decay

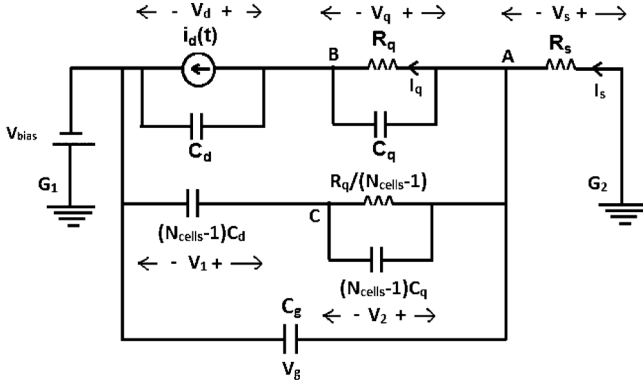


Fig. 2. The equivalent circuit of the SiPM, where the GM-APD is modeled as a current source.

time τ_{md} is also referred to as the quenching time constant and is given by [30], [40]

$$\tau_{md} = C_d \frac{R_d R_q}{R_d + R_q} \quad (2)$$

where R_d and C_d are the reverse-biased diode resistance and capacitance, respectively. For the Hamamatsu multipixel photon counters (MPPCs), $C_d \sim 100$ fF, $R_q \sim 100$ k Ω , and $R_d \sim 1$ k Ω [30] so that $\tau_{md} \sim 100$ ps. If another photon arrives within this time duration, it does not trigger an avalanche. Thus, τ_{md} corresponds to the deadtime of the microcell due to the avalanche being in progress [41].

The GM-APD can be modeled as a voltage source [28], [30], [40] or as a current source [25], [31], [41]. In our analysis, we model the GM-APD as a current source $I_d(t)$ in parallel with a diode capacitance C_d , as shown in Fig. 2. Modeling the GM-APD as a current source helps to model the rise time of the microplasma current accurately. The current source models the total charge delivered by the microcell during a single avalanche event. We define the gain G of the SiPM as the expectation value of the number of output charge carriers due to a single fired cell at the given overvoltage. Then, the total charge due to a single avalanche event is Ge , where e denotes the charge of an electron. As discussed, the delivery of this charge consists of a combination of exponentially rising and decaying pulses. Without loss of generality, assume that the avalanche is triggered at time $t = 0$. Then the expression for $I_d(t)$ is given by

$$I_d(t) = \frac{Ge}{\tau_{md} - \tau_{mr}} \left[\exp\left(\frac{-t}{\tau_{md}}\right) - \exp\left(\frac{-t}{\tau_{mr}}\right) \right] u(t) \quad (3)$$

where $u(t)$ is the unit step function. It can be verified that this expression is correctly normalized and satisfies the initial- and final-value conditions, i.e., at $t = 0$ and at $t = \infty$, $I_d(t) = 0$.

After the avalanche is quenched, the capacitance C_d recharges, leading to the recovery of the diode. If any photon strikes the diode during this recovery phase, it can be detected. However due to the voltage drop across R_q , V_{ob} is less than V_{ob0} . Due to this reduction in V_{ob} , as discussed earlier, the internal QE of the microcell is reduced, leading to a smaller

probability of the photon triggering an avalanche. The gain G of the microcell is also linearly dependent on V_{ob} as [24]

$$G = \frac{(C_d + C_q)V_{ob}}{e} \quad (4)$$

Therefore, due to the reduction in V_{ob} , the output charge produced due to an avalanche when the diode is in its recovery phase is also reduced. As we discuss later, the reduction in V_{ob} also affects other SiPM parameters.

The above-described electrical processes occur in all the microcells when scintillation photons are incident on them. The current pulses generated from the individual microcells add up and are measured by the readout circuit of the SiPM. The voltage drop across any resistance in the readout circuit decreases the value of V_{ob} across all the microcells. This voltage drop V_s can occur in the readout-circuit resistance R_s , as shown in the SiPM-circuit diagram in Fig. 1. Generally there is an amplifier in parallel to the readout-circuit resistance, but due to its high input impedance, its effect on the equivalent resistance is negligible. The voltage drop can also be at the input resistance of a preamplifier and/or the resistance of filter circuitry at the power-supply lines in the readout circuit. Depending on the number of fired cells and the value of the series resistance, the reduction in V_{ob} could be large. This effect is significant when the light levels are high, for example, at the peak of a scintillation pulse. Also, the effect is more pronounced when the light pulse is of the same order of magnitude as the SiPM output pulse duration. Due to the relatively long duration of most scintillation pulses, many scintillation detectors using SiPMs are affected by it [21], [24].

To summarize, the overvoltage across a microcell V_{ob} reduces due to the voltage drops across the quenching resistance R_q and the readout-circuit resistance R_s . Depending on the magnitude of V_{ob} , many microcell parameters are affected. It is thus important to derive accurate expressions for the voltage drops across R_q and R_s , in order to determine V_{ob} accurately at any time following an avalanche. These expressions are also required to determine the transient output response of the SiPM. To compute these voltage drops, we first derive the analytic expression for the current through R_s when only a single microcell fires. We refer to this output as the single-photoelectron response. We then derive the expression for the current through the quenching resistance of the microcell that has fired.

The equivalent circuit of the SiPM when only a single microcell fires, with the fired GM-APD being modeled as a current source, is shown in Fig. 2 [31], [41]. We denote the quenching resistance and capacitance by R_q and C_q , respectively. The reverse-biased diode capacitance is denoted by C_d . The equivalent reverse-biased diode capacitance, quenching resistance and quenching capacitance due to the unfired microcells connected in parallel is given by the circuit elements $C_d' = (N_{cells} - 1)C_d$, $R_q' = R_q/(N_{cells} - 1)$ and $C_q' = (N_{cells} - 1)C_q$, respectively, where N_{cells} denotes the number of microcells in the SiPM. There is also a small parasitic capacitance parallel to each microcell that accounts for the parasitics between the substrate of the device and the contact of the quenching resistor [31]. The combined contribution of all these parasitics is given by the stray capacitance C_g .

Using Kirchhoff's current and voltage laws to analyze this circuit, and transforming the equations to Fourier-domain, we obtain the expression for the single-photoelectron response current $I_s(t)$ across the readout-circuit resistance R_s . The microcell-circuit analysis, shown in Appendix A, yields the expression for $I_s(t)$ as

$$I_s(t) = \frac{1}{2\pi} \int_{-\infty}^{\infty} d\omega \times \frac{I_d(\omega) \exp(j\omega t)(1 + j\omega\tau_2)}{1 + j\omega(\tau_1 + \tau_3 + \tau_4) - \omega^2(\tau_1\tau_4 + \tau_2\tau_3)} \quad (5)$$

where we have defined the following time constants for ease of notation:

$$\tau_1 = R_q(C_q + C_d) \quad (6a)$$

$$\tau_2 = R_q C_q \quad (6b)$$

$$\tau_3 = R_s N_{\text{cells}} C_d \quad (6c)$$

$$\tau_4 = R_s C_g \quad (6d)$$

and where $I_d(\omega)$ is the Fourier transform of the diode current, and from (3), is derived to be

$$I_d(\omega) = \frac{Ge}{(1 + j\omega\tau_{\text{md}})(1 + j\omega\tau_{\text{mr}})}. \quad (7)$$

The integral of (5) is evaluated using contour-integration methods. The derivation is detailed in Appendix B. The final expression for the output current $I_s(t)$ is

$$I_s(t) = Ge \left[a_1 \exp\left(\frac{-t}{\tau_{\text{cd1}}}\right) + a_2 \exp\left(\frac{-t}{\tau_{\text{cd2}}}\right) + a_3 \exp\left(\frac{-t}{\tau_{\text{md}}}\right) + a_4 \exp\left(\frac{-t}{\tau_{\text{mr}}}\right) \right] \quad (8)$$

where the constants $a_1 - a_4$ are defined as below:

$$a_1 = \frac{\tau_{\text{cd1}}(\tau_{\text{cd1}} - \tau_2)}{(\tau_{\text{cd1}} - \tau_{\text{cd2}})(\tau_{\text{cd1}} - \tau_{\text{md}})(\tau_{\text{cd1}} - \tau_{\text{mr}})} \quad (9a)$$

$$a_2 = \frac{\tau_{\text{cd2}}(\tau_{\text{cd2}} - \tau_2)}{(\tau_{\text{cd2}} - \tau_{\text{cd1}})(\tau_{\text{cd2}} - \tau_{\text{md}})(\tau_{\text{cd2}} - \tau_{\text{mr}})} \quad (9b)$$

$$a_3 = \frac{\tau_{\text{md}}(\tau_{\text{md}} - \tau_2)}{(\tau_{\text{md}} - \tau_{\text{cd1}})(\tau_{\text{md}} - \tau_{\text{cd2}})(\tau_{\text{md}} - \tau_{\text{mr}})} \quad (9c)$$

$$a_4 = \frac{\tau_{\text{mr}}(\tau_{\text{mr}} - \tau_2)}{(\tau_{\text{mr}} - \tau_{\text{cd1}})(\tau_{\text{mr}} - \tau_{\text{md}})(\tau_{\text{mr}} - \tau_{\text{cd2}})} \quad (9d)$$

where τ_{cd1} and τ_{cd2} are the roots of the quadratic expression in the denominator of (5). These roots are given by

$$\tau_{\text{cd1}}, \tau_{\text{cd2}} = \frac{\tau_1 + \tau_3 + \tau_4}{2} \pm \frac{\sqrt{(\tau_1 + \tau_3 + \tau_4)^2 - 4(\tau_1\tau_4 + \tau_2\tau_3)}}{2}. \quad (10)$$

The time constants τ_{cd1} and τ_{cd2} are for the exponential decay due to the microcell-circuit elements. We thus have an analytic expression for the single-photoelectron response. We validate that the derived expression is properly normalized by integrating this current from time $t = 0$ to $t = \infty$, to obtain the total output charge that flows through the readout-circuit resistance.

Since all the charge emitted by the GM-APD flows through the readout-circuit resistance, this value should be equal to Ge , and this is verified. The expression for $I_s(t)$ also satisfies the initial- and final-value conditions, namely $I_s(t) = 0$ at $t = 0$ and $t = \infty$. We note that for typical SiPM-circuit parameter values, it can be shown that $\tau_{\text{cd1}} \approx R_q(C_q + C_d)$. This expression is a common approximation for the time constant of the exponential decay due to the microcell-circuit elements [25].

The current across the quenching resistance R_q , denoted by $I_q(t)$, is similarly derived as detailed in Appendix C. The expression for $I_q(t)$ is given by

$$I_q(t) = Ge \left\{ \left[b_1 \exp\left(\frac{-t}{\tau_1}\right) + b_2 \exp\left(\frac{-t}{\tau_{\text{md}}}\right) + b_3 \exp\left(\frac{-t}{\tau_{\text{mr}}}\right) \right] + \frac{\tau_3}{N_{\text{cells}}} \left[b_4 \exp\left(\frac{-t}{\tau_{\text{cd1}}}\right) + b_5 \exp\left(\frac{-t}{\tau_{\text{cd2}}}\right) + b_6 \exp\left(\frac{-t}{\tau_{\text{md}}}\right) + b_7 \exp\left(\frac{-t}{\tau_{\text{mr}}}\right) + b_8 \exp\left(\frac{-t}{\tau_1}\right) \right] \right\} \quad (11)$$

where the constants $b_1 - b_8$ are defined as,

$$b_1 = \frac{\tau_1}{(\tau_1 - \tau_{\text{mr}})(\tau_1 - \tau_{\text{md}})} \quad (12a)$$

$$b_2 = \frac{\tau_{\text{md}}}{(\tau_{\text{md}} - \tau_{\text{mr}})(\tau_{\text{md}} - \tau_1)} \quad (12b)$$

$$b_3 = \frac{\tau_{\text{mr}}}{(\tau_{\text{mr}} - \tau_1)(\tau_{\text{mr}} - \tau_{\text{md}})} \quad (12c)$$

$$b_4 = \frac{\tau_{\text{cd1}}(\tau_{\text{cd1}} - \tau_2)}{(\tau_{\text{cd1}} - \tau_{\text{cd2}})(\tau_{\text{cd1}} - \tau_1)(\tau_{\text{cd1}} - \tau_{\text{md}})(\tau_{\text{cd1}} - \tau_{\text{mr}})} \quad (12d)$$

$$b_5 = \frac{\tau_{\text{cd2}}(\tau_{\text{cd2}} - \tau_2)}{(\tau_{\text{cd2}} - \tau_{\text{cd1}})(\tau_{\text{cd2}} - \tau_1)(\tau_{\text{cd2}} - \tau_{\text{md}})(\tau_{\text{cd2}} - \tau_{\text{mr}})} \quad (12e)$$

$$b_6 = \frac{\tau_{\text{md}}(\tau_{\text{md}} - \tau_2)}{(\tau_{\text{md}} - \tau_{\text{cd1}})(\tau_{\text{md}} - \tau_1)(\tau_{\text{md}} - \tau_{\text{cd2}})(\tau_{\text{md}} - \tau_{\text{mr}})} \quad (12f)$$

$$b_7 = \frac{\tau_{\text{mr}}(\tau_{\text{mr}} - \tau_2)}{(\tau_{\text{mr}} - \tau_{\text{cd1}})(\tau_{\text{mr}} - \tau_1)(\tau_{\text{mr}} - \tau_{\text{md}})(\tau_{\text{mr}} - \tau_{\text{cd2}})} \quad (12g)$$

$$b_8 = \frac{\tau_1(\tau_1 - \tau_2)}{(\tau_1 - \tau_{\text{cd1}})(\tau_1 - \tau_{\text{cd2}})(\tau_1 - \tau_{\text{md}})(\tau_1 - \tau_{\text{mr}})}. \quad (12h)$$

The expression for $I_q(t)$ also satisfies the initial- and final-value conditions. In the results section, we further validate the above-derived expressions using circuit-simulation techniques. We note that for typical values of the above-defined time constants in a SiPM, we can approximate the expression for $I_q(t)$ to

$$I_q(t) \approx \frac{Ge}{\tau_1} \exp\left(\frac{-t}{\tau_1}\right) \quad (13)$$

which is a commonly used approximation for the current across the quenching resistance [21], [24]. To determine the net output charge from the SiPM, we can add the output from individual microcells as long as we consider the effect of the voltage drop

across the readout-circuit resistance on the overvoltages across the triggered microcells [30].

B. Afterpulsing

We define afterpulsing as the number of additional triggers in the same cell per original avalanche [24]. The probability distribution of the number of afterpulses originating from a single avalanche can be described by a Poisson distribution with mean \bar{N}_{ap} [24] at $V_{ob} = V_{ob0}$. We denote the time between the triggering of the avalanche causing the afterpulse and the triggering of the afterpulse by Δt . For each trapped charge carrier that initiates an additional avalanche, the probability distribution of Δt , which we denote by $\lambda_{ap}(\Delta t)$, can be described as a sum of multiple exponentials with time constants ranging from 10^{-8} to 10^{-5} seconds [42], [43]. It has been shown that we need to consider at least two of these exponentials to model the afterpulse phenomenon accurately [26], [42], [43], so that

$$\lambda_{ap}(\Delta t) = \frac{\bar{n}_{apf}}{\tau_{apf}} \exp\left(-\frac{\Delta t}{\tau_{apf}}\right) + \frac{\bar{n}_{aps}}{\tau_{aps}} \exp\left(-\frac{\Delta t}{\tau_{aps}}\right) \quad (14)$$

where τ_{apf} and τ_{aps} denote the time constants of the fast and slow components of the afterpulse, while \bar{n}_{apf} and \bar{n}_{aps} correspond to the average number of fast and slow afterpulses, respectively, so that their sum is equal to \bar{N}_{ap} . The probabilities of the short and long afterpulses are almost equal to each other [21]. The number of afterpulse events due to an avalanche is proportional to the amount of charge produced in the avalanche, which is dependent on the overvoltage. Therefore, the probability of afterpulsing is dependent on the overvoltage [21], [24], [43]. It has been observed experimentally that for the Hamamatsu MPPC S10362-11-050C, the probability of afterpulsing depends on the overvoltage quadratically, and the time constants and the amplitude of the short component of the afterpulse decrease with temperature [21], [43].

C. Optical Crosstalk

During an avalanche, there can be emission of optical photons that may reach other cells and trigger additional avalanches. Consequently, two or more pixels can fire almost simultaneously, on the time scale of 1 ns [21]. This process is known as optical crosstalk [43]. Since this is a rare binomial process, the probability distribution of the number of crosstalk events due to a given avalanche is described by a Poisson distribution with mean \bar{N}_{oct} . We note that our definition of \bar{N}_{oct} includes only the primary crosstalks that occur from an original avalanche, and not the secondary crosstalks caused due to the primary crosstalks. Since the number of optical cross-talk events is proportional to the amount of charge produced due to the avalanche, which in turn is proportional to the overvoltage, therefore, the probability of optical crosstalk events varies with overvoltage [22], [24]. For the Hamamatsu MPPC S10362-11-050C, it has been observed that the probability of number of optical crosstalk events varies with overvoltage quadratically [21], [22], [43].

D. Dark Counts

Ideally a SiPM should produce no response in dark conditions. However, in practice, the seed carriers can be generated

not only by optical excitations, but also by other mechanisms, such as the thermal generation of carriers due to the generation-recombination processes within the semiconductor and tunneling effects [44]. These charged carriers can then enter the Geiger multiplication region and trigger avalanches that are referred to as dark counts. Let r_{dc} denote the total dark count rate of the SiPM and Δt_{meas} denote the total measurement time. Then the number of dark counts are described by a Poisson distribution with mean \bar{N}_{dc} at V_{ob0} such that

$$\bar{N}_{dc} = r_{dc} \Delta t_{meas}. \quad (15)$$

The dark count rate r_{dc} varies linearly with overvoltage [21], [22] and exponentially with temperature [21].

III. SIMULATION OF SiPM RESPONSE

As we discussed, the SiPM parameters are all dependent on overvoltage across the microcell, which in turn, depends on the voltage across the quenching and readout-circuit resistances. The triggering of an avalanche is an asynchronous event. After an avalanche event occurs in a microcell, the voltage drop across the quenching resistance varies considerably due to the high value of this resistance. This voltage drop has a significant effect on the SiPM microcell parameters. To model the asynchronous avalanche event accurately, we simulate the triggering of an avalanche as a discrete-event process. Conversely, the readout-circuit resistance is typically much smaller in comparison to the quenching resistance. Therefore, the voltage drop across the readout-circuit resistance is not as significant and immediate as the voltage-variation across the quenching resistance. Moreover, this voltage drop is also dependent on the avalanches that occur in all the microcells. Modeling the voltage drop variation across the readout circuit as a coarsely sampled discrete-time process is therefore computationally fast and relatively accurate. Because of the dual nature of the simulation mechanisms involved, we model the processes in the SiPM using a combined discrete-time discrete-event framework.

A flow chart of the simulation code for a single trial of the MC simulation is shown in Fig. 3. In Fig. 4, we show the various time notations that are used to describe the simulation mechanism. The simulation starts with reading the input parameters: the measured and fixed parameters of the SiPM, experimental-setup parameters, and the timestamps of all the scintillation photons. Depending on the scintillator decay time, we generate multiple non-uniform-duration time steps such that the number of photons in all the time steps is approximately uniform. We denote the time at which the m th time step starts by T_m .

For each photon incident on the SiPM, we first determine the time step it belongs to. We then find the microcell that the photon hits by sampling the spatial distribution of the incident light. Since the size of the SiPM is small, we assume a uniform spatial distribution of the photons on the SiPM, but if there is non-uniform spatial distribution, our model can easily account for that. Next, we consider the internal QE of the SiPM at V_{ob0} and via binomial sampling, determine if the incident photon can cause an avalanche. This results in a list of “potential” photon-triggered avalanches. Similarly, we consider the dark current rate r_{dc} at V_{ob0} and thus find the potential dark count

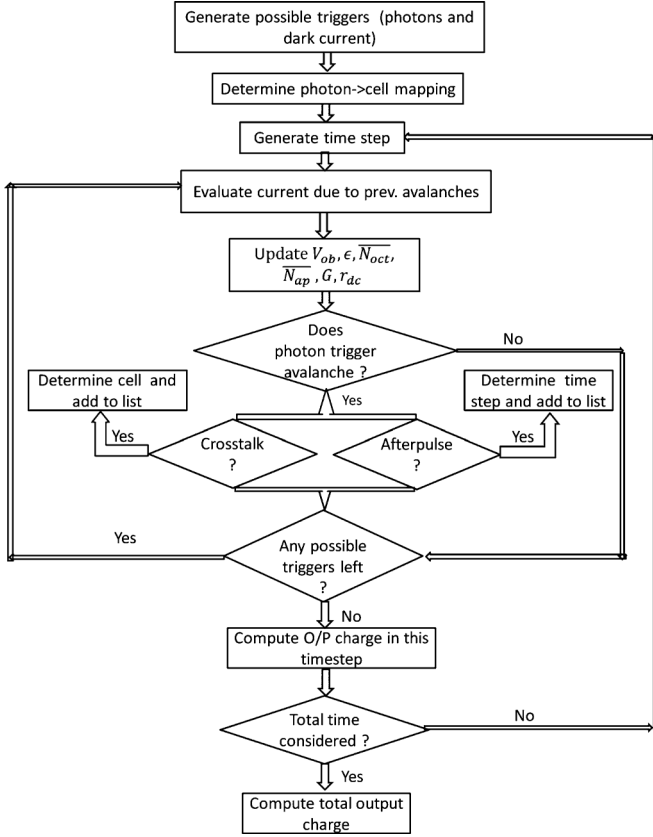


Fig. 3. Flowchart of our simulation technique.

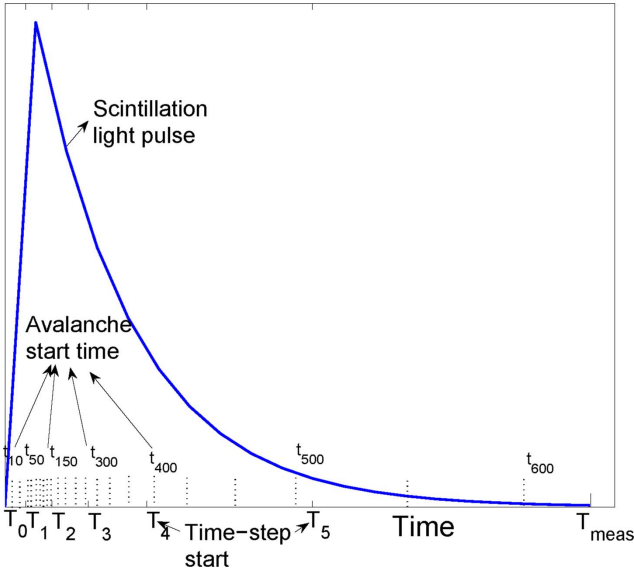


Fig. 4. The various time-based notations used in our flowchart. The figure provides only a rough representation of the time scales involved.

events. We also add them to the list of potential avalanches. One of the main data structures in our software, thus, is the list of potential avalanches. This data structure consists of four elements: the time-stamp of the potential avalanche, the type of avalanche it could be, i.e., photon-, dark-count-, afterpulse- or optical crosstalk-triggered, the microcell index of the potential avalanche, and the amount of charge that the triggering of this potential avalanche would eventually cause. Another main data structure in our simulation code is the microcell data structure.

This data structure consists of two elements: the list of the timestamps of the avalanches that have occurred in a given microcell during a given time step, and the amount of charge that the triggering of the avalanche caused. Any potential avalanche in this list that is separated in time from the previous potential avalanche by a value less than the dead time of the detector τ_{ind} (2) is removed.

At this stage in our simulation, we have the list of potential photon- or dark count-triggered avalanches. For the k th potential avalanche initiated at time t_k , we know its microcell index, which we denote by i_k . Let us assume that this avalanche belongs to the m th time step. Using (11), we determine the current flow at time t_k through the quenching resistance due to all the previous avalanches that have occurred in the i_k th microcell. We thus compute the voltage drop across the quenching resistance of the i_k th microcell at time t_k due to all the previous avalanches in this microcell. We denote this voltage drop by $V_q^{i_k}(t_k)$. The effective overvoltage across the i_k th microcell at time t_k , which we denote by $V_{\text{ob}}^{i_k}(t_k)$, is then computed by subtracting the sum of diode-breakdown voltage V_{br} , voltage drop across quenching resistance at time t_k , $V_q^{i_k}(t_k)$, and the voltage drop across the readout-circuit resistance at the beginning of the m th timestep, $V_s(T_m)$, from the bias voltage V_{bias} . Since $V_{\text{ob}}^{i_k}(t_k)$ affects the gain, internal QE, dark count probability and other SiPM parameters of the i_k th microcell, we recompute these SiPM parameters based on the relation between these parameters and the overvoltage. We then check if the potential photon- or dark count-triggered avalanche can actually occur, given the updated values of internal QE and dark count probability, respectively. This is done by computing the ratio of the updated parameter value at overvoltage $V_{\text{ob}}^{i_k}(t_k)$ and the parameter value at the overvoltage $V_{\text{ob}0}$, followed by performing a binomial sampling with this ratio as the probability of occurrence of the potential avalanche. If the potential avalanche occurs, using the recomputed-gain value, the charge parameter in the data structure corresponding to this avalanche is updated.

Next, we determine if this k th triggered avalanche can cause afterpulsing events. Afterpulsing is an inhomogeneous-intensity Poisson point process, with intensity function $\lambda_{\text{ap}}(\Delta t)$ (14). Therefore, we first sample a number N_{ap} from a Poisson distribution with the updated mean $\bar{N}_{\text{ap}}(V_{\text{ob}}^{i_k}(t_k))$. We then sample N_{ap} time values from a distribution corresponding to the normalized version of $\lambda_{\text{ap}}(\Delta t)$, using which the occurrence-time of the afterpulsing events can be determined to be $t_k + \Delta t$. Depending on their time of occurrence, the afterpulsing events are inserted into the list of potential avalanches. Any afterpulsing events that occur within the dead time interval in the considered microcell are removed.

We then determine if this avalanche can trigger an optical crosstalk by sampling N_{oct} from a Poisson distribution with the updated-mean $\bar{N}_{\text{oct}}(V_{\text{ob}}^{i_k}(t_k))$. It is assumed that only the neighboring microcells are affected by this crosstalk [21], [26], [32], [45], and that the photon emission is isotropic so that each of the four neighboring microcells have a uniform probability of being triggered by the optical crosstalk. Optical crosstalk is considered to occur about 1 ns after the original avalanche [21]. All the optical crosstalk events are also added to the list of potential avalanches. Using this framework, we can model

TABLE I
ESTIMATED MICROCELL-CIRCUIT-ELEMENT VALUES FOR HAMAMATSU MPPC S10362-33-050C AND THE OTHER SIMULATION PARAMETERS

Parameter	C_q	C_d	C_g	R_q	R_s	V_{ob0}	τ_{md}	τ_{mr}
Value	23 fF	77 fF	28 pF	140 k Ω	15 Ω	1.33 V	100 ps	10 ps

afterpulsing and crosstalk causing secondary crosstalk or afterpulsing events, up to any order.

The process is repeated for all the avalanches in the list in the given time step. After we have analyzed all the potential avalanches in the m th time-step, at the time corresponding to the end of the time-step, i.e., T_{m+1} , the current flow through R_s due to all the avalanches that have occurred in the m th and all previous time-steps is computed using (8). Using this, the voltage drop across R_s at time T_{m+1} is determined. As a result, at the beginning of the next time step, the voltage drop across R_s is known. Following this, all the potential avalanches in the next time step are considered. This process is continued for all the time steps until the measurement time expires. At the end of a single trial of this MC simulation, we have the list of all the triggered avalanches, along with their time stamps and the amount of charge flow due to them. Using this information, we can determine the total output charge through the SiPM, or if required, determine the output waveform using (8). We can run this simulation multiple times to determine the mean and variance of the SiPM output.

For each simulation trial, we require the different measured parameters of the SiPM, such as the electrical-circuit parameters, the gain, internal QE, and the afterpulsing and crosstalk probabilities. The value of these parameters can be determined from experiments as mentioned in [21], [24], [26], [30], but these values can have measurement uncertainties. To model this uncertainty, we assume that the measurement errors are normally distributed with zero mean and variances given by the variances of the experimentally determined values. We have assumed a zero-mean normal distribution for the measurement error since it is the most commonly used model to characterize such errors. However, an alternative distribution can be easily incorporated. The sampled value of the error is added to the mean of the experimentally determined value and thus, the SiPM parameter is determined for the simulation trial.

As mentioned earlier, we simulate the SiPM as a discrete-time process to account for the variation in voltage across the readout-circuit resistance during one scintillation pulse. To ensure that the simulation is stable with respect to the number of time steps, we divide the total measurement-time duration such that the number of photons in the different time steps are similar. We keep the number of time steps as an input parameter to the simulation so that it could be optimally set by the end user. This parameter should be kept reasonable so that the continuous variation in output voltage is modeled accurately and efficiently. An optimum number of time steps can be obtained for a given configuration by determining the number of time steps at which the SiPM output converges. Our scheme of non-uniform division of measurement time should help the convergence occur within a smaller number of time steps, thus improving the computational efficiency of the software.

There are some dependencies between the SiPM parameters and factors such as overvoltage and temperature, which do not have an analytical form. However often the SiPM end users have experimental data that can describe these dependencies. In the presence of such experimental data, to simulate the corresponding dependency, we implement a lookup-table approach. The end-user inputs the paired-measurement values, i.e., the value of the factor causing the SiPM-parameter variation, and the corresponding SiPM parameter value. Using these measurements and a splines-based interpolation technique, the value of the SiPM parameter is computed for the required value of the factor causing the SiPM parameter variation.

Finally, we also provide an interface in the software to turn off the effects of different phenomena in the SiPM. The interface helps to study the effect of different phenomena individually, measure certain SiPM parameters, design front-end electronics for SiPM-based detectors and perform sensitivity analysis. The simulation framework has been implemented using Matlab (Mathworks, Natick, Mass.).

IV. EXPERIMENTS AND RESULTS

A. Validating the Single-Photoelectron Response

In Section II-A, we verified that the derived expressions for the single-photoelectron response (8), and the current through the quenching resistor (11) were correctly normalized. To further validate these analytic expressions, we simulate the equivalent circuit of the microcell of the SiPM (Fig. 2) using LTSpice IV [46]. LTSpice IV is a schematic-driven circuit-simulation program originally based on Berkeley SPICE 3F4/5. We simulate the microcell of the Hamamatsu MPPC S10362-33-050C device using LTSpice IV. The circuit parameters for the microcell of this device were estimated based on test measurements, and are given in Table I. The table also lists the other parameter values that we use in the circuit simulation.

The current through the readout-circuit resistance R_s is simulated and compared to the output obtained using (8). The result is shown in Fig. 5. Similarly, the current through the quenching resistance R_q is simulated using LTSpice IV and compared to that obtained using (11). The result is shown in Fig. 6. We observe that, for both the single-photoelectron response and the current through the quenching resistance, the analytic and simulated outputs match each other. This further confirms the correctness of the derived expressions.

B. Validating the MC Model

1) *Simulation Setup*: To verify the accuracy of our MC model to simulate SiPM response to scintillation light, we consider different test cases. The simulation setup for these test cases is similar to the experimental setup in Van Dam *et al.* [24]. In this experimental setup, several isotopes such as I-125,

TABLE II
MEASURED SiPM PARAMETER VALUES FOR THE TWO HAMAMATSU S10362-33-050C DEVICES. ALL UNCERTAINTIES QUOTED ARE 95% CONFIDENCE INTERVALS, BASED EITHER ON FITS OR ON ESTIMATED MEASUREMENT UNCERTAINTIES. SOURCE [24]

Detector	$V_{ob0}(V)$	$R_q(k\Omega)$	$G(10^5)$	\bar{N}_{ap}	$\tau_{ap}(ns)$	$r_{dc}(MHz)$	\bar{N}_{oct}
Detector 1	1.26 ± 0.05	145.3 ± 0.5	8.3 ± 0.5	0.124 ± 0.005	25 ± 8	5.6 ± 0.1	0.140 ± 0.005
Detector 2	1.39 ± 0.05	140.4 ± 0.5	7.9 ± 0.5	0.132 ± 0.005	26 ± 8	5.1 ± 0.1	0.132 ± 0.005

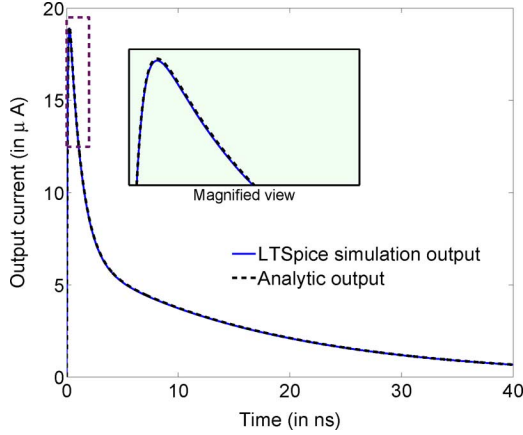


Fig. 5. The single-photoelectron response of a SiPM determined using our analytic expression compared with that simulated using LTSpice.

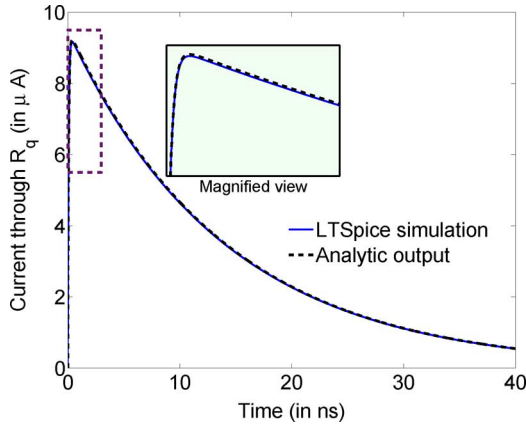


Fig. 6. The current across the quenching resistance of the SiPM when only one microcell has fired, determined using our analytic expression and compared with that simulated using LTSpice.

Am-241, Hg-203, Na-22, Cs-137, Y-88, and Co-60 are used which emit gamma-ray photons at ten different energies between 27.3 and 1836 keV. The gamma-ray photons are incident on two LaBr₃:5%Ce scintillators that are optically coupled to their respective Hamamatsu MPPC S10362-33-050C SiPMs using a Silicone encapsulation gel. The scintillation photons from the scintillators are incident on their respective SiPMs, and each SiPM produces an output charge. This output is expressed in terms of the single-photon-avalanche response parameter χ [24], which gives a measure of the mean number of equivalent microcells that fire per photon-triggered avalanche. Let N_{ph} denote the number of scintillation photons emitted by the scintillator. As mentioned earlier, ϵf is the detector PDE, so that $\epsilon f N_{ph}$ is the mean number of photon-triggered avalanches. Also, let $\bar{N}_{f,eq}$ denote the mean output charge from the SiPM in

terms of the equivalent number of fired cells, which is defined as the total output charge divided by the charge due to single fired microcell. Then the parameter χ is defined as

$$\chi = \frac{\bar{N}_{f,eq}}{\epsilon f N_{ph}}. \quad (16)$$

Since χ is the ratio of the mean number of fired cells per photon-triggered avalanche, the value of χ is an indicator of SiPM saturation. In theory, the value of χ should be one when the device operates in the pure linear regime and we do not consider the noise effects. However, when SiPM saturation occurs, the value of χ will be less than one. Afterpulse, crosstalk, and dark current can cause the value of χ to be greater than one when there are no saturation effects.

2) *SiPM Parameter Values and Other Simulation Parameters*: To determine the SiPM parameters in each trial of the MC simulation, we use the mean and standard deviation values determined experimentally in Van Dam *et al.* [24], which are listed in Table II. For the sake of consistency, in each trial, we compute the time constant τ_1 from the values of G , R_q and V_{ob0} using the relation

$$\tau_1 = \frac{GeR_q}{V_{ob0}}. \quad (17)$$

This relation can be derived using (4) and (6a). Also, for the various capacitances in the SiPM microcell circuit, we use the values listed in Table I. We keep the value of the readout-circuit resistance R_s and the measurement time as 15 Ω and 500 ns, respectively, which are the same values as in the experimental setup.

The detector PDE ϵf is difficult to measure directly since it depends on factors such as detector geometry, scintillator, and the use of reflecting materials. Therefore, to determine the detector PDE ϵf , we use the experimental output that is least influenced by saturation, i.e., the measurement at 27.3 keV. This experimental output is obtained from Van Dam *et al.* [24]. We find the value of ϵf so as to match the modeled and measured response at 27.3 keV. Using this method, we obtain the detector PDE values for Detectors 1 and 2 to be 0.157 and 0.172, respectively.

With regard to SiPM-parameter variation with overvoltage, we assume that the value of gain and dark count rate decrease with decreasing overvoltage linearly, and the values of \bar{N}_{ap} and \bar{N}_{oct} decrease with decreasing overvoltage quadratically [21], [26]. We model the variation in detector PDE with overvoltage using the experimental measurements obtained in Retière *et al.* [21].

3) *Comparison With Experimental Output*: We first compare the response predicted from the MC model to actual experimental output. We simulate the experimental setup as described

in Section IV-B1 and obtain the response of the two SiPMs for different isotopes, which correspond to the different number of emitted photons. The actual experimental output for this setup is obtained from Van Dam *et al.* [24].

In Fig. 7, the results from our simulation are plotted along with the experimental output. The error bars denote the variance in the single-photon-avalanche response of the simulated output. We notice that the simulated results are close to the experimental output. The Pearson's correlation coefficient between the mean value of the experimental and simulated outputs is greater than 0.99 for both the detectors. There is some discrepancy between the two results that can be due to error in some of the measured parameters, especially the gain G . Estimating G involves measuring the small signals resulting from only a few photons. Because of this and the high capacitance of the 3 mm \times 3 mm Hamamatsu S10362-033C, noise increases the difficulty in estimating G . The consequences of an error in measuring G are significant, since apart from introducing error in the value of the charge due to an avalanche, it also causes an error in the computed values of voltages across quenching and readout-circuit resistances. This in turn affects the computed overvoltage across the microcell, which leads to incorrect update of the various SiPM parameters during the recovery phase of the microcell. Another possible source of discrepancy is that to determine the detector PDE, we fit the model to the measurements at low gamma-ray energies. The photons at low energy values, however, are absorbed in the top few-tenths mm of the crystal and can have a different detector PDE than the high-energy gamma-ray photons that are absorbed throughout the crystal. This depth-of-interaction effect can result in the detector PDE being different for different energy of gamma-ray photons. Also, to evaluate the dependency of the various SiPM parameters on overvoltage for the SiPMs in this experiment [24], we used the expressions that were obtained from other experimental setups [21], [26]. However, the relationships between the SiPM parameters and overvoltage might vary for different SiPMs, leading to another source of error. In fact, we observed that when we do not model the decrease in PDE with overvoltage, the experimental and MC outputs match very well. Another reason for the discrepancy can be that we assume a uniform light distribution on the SiPM, an assumption that might not be completely valid. There are also some other reasons for the discrepancies in the measured SiPM parameters, which are mentioned in detail in Van Dam *et al.* [24], and due to these errors, some mismatch between the MC and experimental output can be expected. Thus, the comparison with experimental results is more of a best-effort task to validate the MC model. To validate the model further, we perform more simulation experiments that constrain the data.

In the simulation experiments that follow, the setup is the same as the experimental setup, with the exception that only one scintillator-SiPM detector pair is considered. The considered SiPM detector has parameters as listed for Detector 1 in Table II.

4) *Comparison With Known Cases:* We compare the model output with cases for which the single-photon-avalanche response is known theoretically and *a priori*. The first case where the SiPM response is known *a priori* is when the source is an

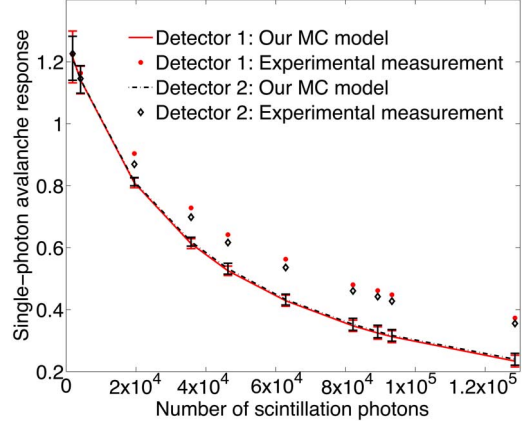


Fig. 7. The predicted-SiPM output, expressed in terms of single-photon-avalanche response, as a function of the emitted photons from the scintillator, compared with the experimental output obtained from Van Dam *et al.*, [24]. The error bars denote the standard deviation of the single-photon-avalanche response in our MC-model output. Note that although we use our MC model to predict the output at only those points at which the experimental output is known, the MC model can be used to predict the output for any number of scintillation photons.

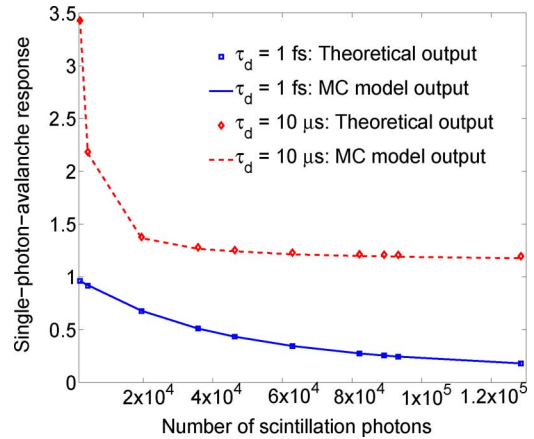


Fig. 8. Evaluating the MC model in cases where the single-avalanche-photon-response is known theoretically and *a priori*.

almost instantaneous light pulse (decay time = 1 fs), with no afterpulsing and optical crosstalk effects in the SiPM. The value of χ for this case is well known mathematically and is given by a simplified exponential model [47]

$$\chi = \frac{N_{\text{cells}}}{\epsilon f N_{\text{ph}}} \left[1 - \exp \left(-\frac{\epsilon f N_{\text{ph}}}{N_{\text{cells}}} \right) \right]. \quad (18)$$

As we observe in Fig. 8, the output from our simulation matches with the above-known mathematical model. This result demonstrates the validity of the model in a case where saturation is predominant.

The second case where the SiPM response is known *a priori* is for a scintillator with a decay time much longer than the time duration of any of the transient effects in the SiPM. In this case, the SiPM microcells fully recover before being triggered by another scintillation photon. However, since afterpulsing occurs within a small duration in the same cell in which the photon-triggered avalanche occurs, the afterpulsing event is still affected

due to the non-recovery of the microcell. If we neglect the effect due to afterpulsing, the SiPM output is not affected due to saturation effects, or alternatively, the output is linear to the avalanche-causing effects. Considering the occurrence of optical crosstalk up to any order, the SiPM output is given by an infinite geometrical series. In this case, we can derive the SiPM output expression in terms of the equivalent number of fired cells as

$$\bar{N}_{f,eq} = \frac{\epsilon f \bar{N}_{ph} + r_{dc} \Delta t_{meas}}{1 - \bar{N}_{oct}}. \quad (19)$$

Consequently, we can obtain the expression for χ using (16) as

$$\chi = \frac{1}{1 - \bar{N}_{oct}} \left(1 + \frac{r_{dc} \Delta t_{meas}}{\epsilon f \bar{N}_{ph}} \right). \quad (20)$$

To validate this case, we consider a scintillator with a decay time $\tau_d = 10 \mu s$ as the light source in the simulation setup, and turn off the afterpulsing phenomena in the simulation. We observe in Fig. 8 that the value of χ obtained from the MC model matches well with the expected theoretical response. We also note that the value of χ is not a constant. This is due to dark current, which, at low photon counts, is comparable to the total number of photon-triggered avalanches. Consequently, the term $(r_{dc} \Delta t_{meas}) / (\epsilon f \bar{N}_{ph})$ in the expression for χ is significant at low photon counts. This result demonstrates the validity of the MC model in an extreme case where the SiPM is operating in a completely linear regime.

5) *Effect of Different SiPM Phenomena*: To further validate the model, we study the effect of specific phenomena in the SiPM and observe if the predicted output is expected.

a) *Varying Readout-Circuit Resistance*: In this experiment, we study the SiPM response as the readout-circuit resistance value is varied from 1Ω to 500Ω . We observe from the results shown in Fig. 9 that as the readout-circuit resistance increases, the value of χ reduces. This is expected since an increase in the output resistance leads to an increase in the output voltage drop across the readout circuit, which in turn leads to a decrease in the overvoltage across the microcells. Thus the SiPM gain and detector PDE are reduced for the photons arriving in the recovery phase. Moreover, the recovery time of the SiPM, which depends on the value of R_s ((6c) and (6d)) also increases, thus leading to increase in SiPM saturation, and thus a decrease in the value of the χ parameter. We would like to mention here that the experiment of varying readout-circuit resistance with a fast and high-light-yield scintillator such as LaBr₃:5%Ce provide a relatively easy method to validate the R_s dependency of the developed MC model.

b) *Varying Overvoltage*: In the second experiment, we study the SiPM response as the externally applied initial overvoltage V_{ob0} is varied. The results are presented in Fig. 10, and we observe that as V_{ob0} increases, the single-photon-avalanche response becomes smaller, indicating that the SiPM saturation is higher for higher overvoltages. This is expected since as the overvoltage increases, the detector PDE, dark current rate, and the afterpulsing and crosstalk probability increase. This leads to a higher number of triggered avalanches, due to which saturation effects increase. Moreover, at higher overvoltage, the gain is higher, and this also leads to more saturation.

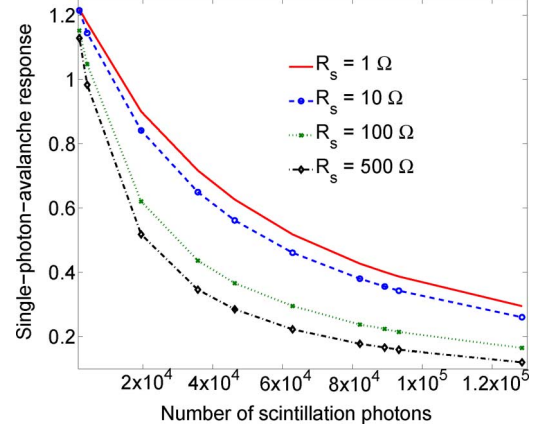


Fig. 9. Effect of varying the readout-circuit resistance on the SiPM output.

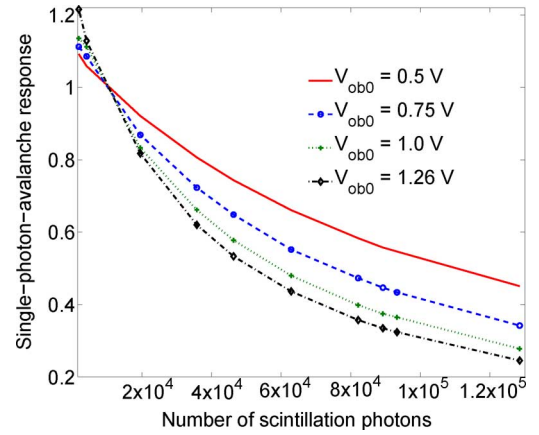


Fig. 10. Effect of varying the overvoltage on the SiPM output.

c) *Turning Off Certain SiPM Phenomena*: In this experiment, we turn off the effect due to certain SiPM phenomena in the simulation. This can be easily done using a flag that is provided as a user input. We first turn off the effect due to afterpulsing and optical crosstalk processes. We observe that the predicted-SiPM output reduces in this case, and this reduction is more pronounced at low photon counts, as shown in Fig. 11. Also, at low photon counts, the predicted value of χ is equal to unity in the absence of crosstalk and afterpulse. In another experiment, we turn off the variation in detector PDE due to variation in overvoltage. We observe, from the result shown in Fig. 11, that the SiPM output increases in this case. All these results are expected and help validate the model further.

d) *Sensitivity Analysis*: In this experiment, we study the sensitivity of the SiPM output to the measured detector PDE value. We choose three detector PDE values, 0.125, 0.15 and 0.175, and obtain the SiPM output for each of these detector PDE values using the MC model. We plot the value of χ as a function of the number of emitted photons in Fig. 12. We also plot the standard deviation of χ since it indicates the precision of the predicted MC output, which is required in this analysis. We observe that, as expected, an increase in the detector PDE leads to increased saturation. Sensitivity analysis such as these can help an end-user determine the effect of error in any measured

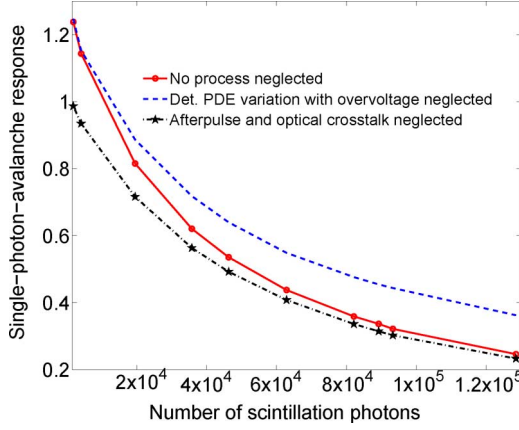


Fig. 11. Effect of neglecting two SiPM phenomena, the PDE variation with overvoltage, and the optical crosstalk (OCT) and afterpulsing (AP) effects, on the predicted-SiPM output.

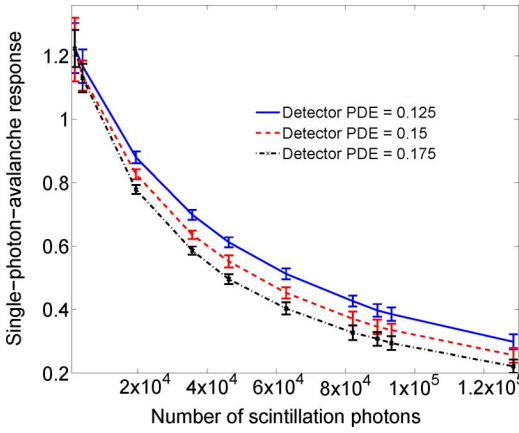


Fig. 12. Effect of varying the detector PDE on the SiPM output. The error bars denote the standard deviation in the value of χ .

SiPM parameter. They can also indicate whether the coarse estimation of a SiPM parameter is sufficient to compute SiPM response in comparison to an accurate estimation. This is helpful if an end-user is considering whether to use an approximate value for a certain SiPM parameter, or instead design an experimental setup and measure the parameter accurately.

6) *Predicting Response to Different Scintillators:* We use the MC model to predict the SiPM response to four different scintillators, viz. $\text{LaBr}_3\text{:5\%Ce}$, LYSO, NaI:Tl , and BGO, irradiated with gamma-ray photons of energy 511 keV, as used in PET. Each of these scintillators has different decay times and different light yields [48], [49], as listed in Table III. Since the detector PDE, ϵf , depends on factors such as detector geometry and the use of reflecting materials, we compute the response as a function of the detector PDE.

We plot the results for this experiment in Fig. 13. We observe that for the low-light-yield BGO scintillator, saturation is not really a significant issue. For NaI:Tl and LYSO, which have higher light yield and smaller decay time than BGO, saturation effects are more pronounced and the value of χ is less than unity when the detector PDE is high. $\text{LaBr}_3\text{:5\%Ce}$, which is the fastest and highest light-yield among the four scintillators is affected most by saturation.

TABLE III
PROPERTIES AND COMPUTATIONAL-TIME REQUIREMENTS
FOR THE DIFFERENT SCINTILLATORS

Quantity	$\text{LaBr}_3\text{:5\%Ce}$	LYSO	NaI:Tl	BGO
Decay time (ns)	16	41	250	300
Light Yield (ph/keV)	70	27	53	6.3
Computational time (sec)	20	9.2	17.4	3.2

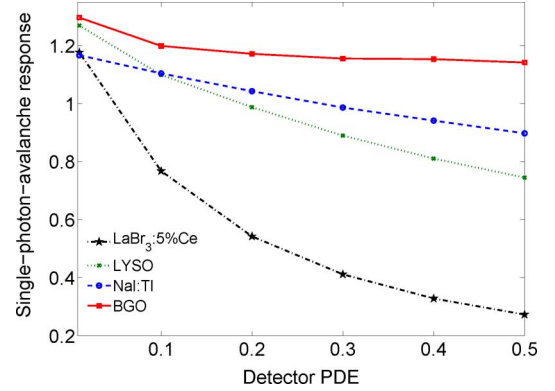


Fig. 13. Predicting the response to different scintillators using the MC model.

We also observe that the value of χ for BGO is higher at lower detector PDE values than at the higher detector PDE values. This is due to the higher relative contribution of dark current at low detector PDE values to the total output charge. We also note that at low detector PDE value, the value of χ is higher for low-light-yield scintillators such as BGO and LYSO as compared to the high-light-yield scintillators such as $\text{LaBr}_3\text{:5\%Ce}$ and NaI:Tl . This is because computing the value of χ requires a division by $\epsilon f \bar{N}_{\text{ph}}$ (16). This term is smaller for low-light-yield scintillators, due to which the relative contribution of the dark current term (15) to the value of χ , i.e., $(r_{\text{dc}} \Delta t_{\text{meas}}) / (\epsilon f \bar{N}_{\text{ph}})$, becomes significant. Thus, all the observations are expected, further validating the model.

C. Computational Time Requirements

To evaluate the computational time requirements of the developed software, and to study the dependency of the output on the number of timesteps in the simulation, we conduct two sets of experiments on a system consisting of two quad-core Intel Xeon 2.26 GHz processors running 64 bit Linux. In the first experiment, we have the same general simulation setup as described at the beginning of Section IV-B with a $\text{LaBr}_3\text{:5\%Ce}$ crystal and a SiPM detector with the same parameters as Detector 1 in Table II. The experiment is run with four different values for the number of timesteps, which are 1, 10, 20, and 25, respectively. The SiPM output with 25 timesteps is considered to be an approximately true value of the output since on increasing the number of timesteps further, the SiPM output changes by only a very small amount. Using this output as the true value, the absolute value of the error in the output when 1, 10 and 20 timesteps are considered, is evaluated and plotted as a function of the number of scintillation photons in Fig. 14(a). We observe that on increasing the number of timesteps from 1 to 10, the error in the output reduces significantly. A further increase

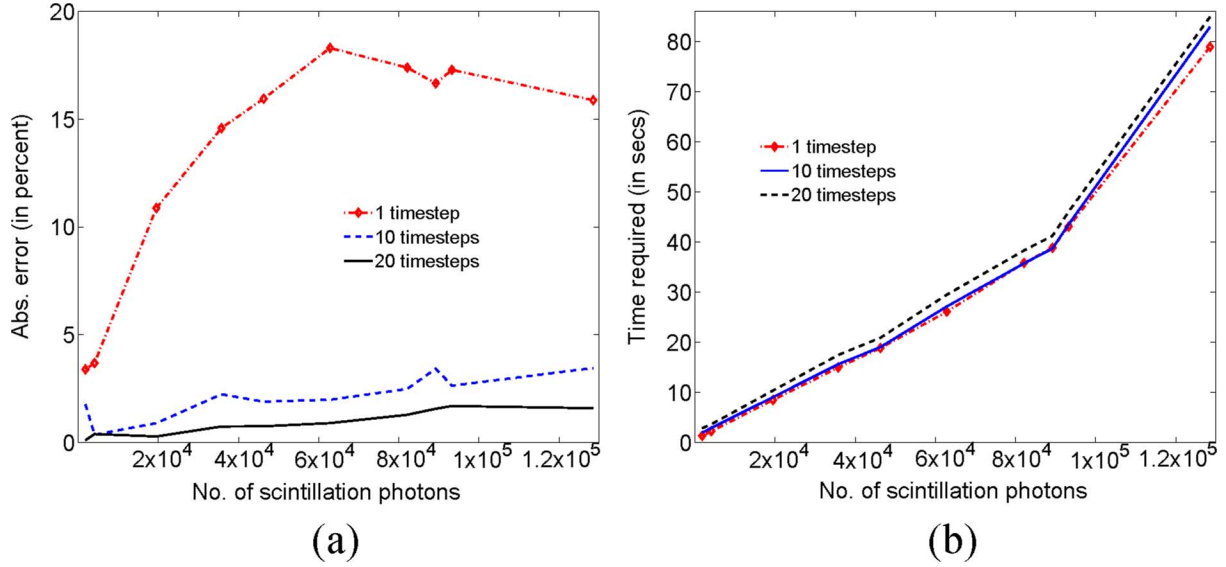


Fig. 14. (a) The error in the SiPM output as the number of timesteps is varied, plotted against the number of incident photons. (b) The computational time required by the software for one MC trial, for different number of timesteps, as the number of incident photons increases.

in the number of timesteps causes a minor decrease in the error. Thus we observe the convergence of the simulation output as the number of timesteps increases. In Fig. 14(b), the computational time required by the software for one trial of the MC simulation, and 1, 10, and 20 timesteps is plotted as a function of the number of scintillation photons. We observe that as the number of incident photons increases, the computation time increases almost linearly. Also, increasing the number of timesteps does not have a significant effect on the computational time requirements of the software.

In the second experiment, we have the simulation setup as in Section IV-B6. The computational time required by one trial of the MC simulation, when the detector PDE value is 0.2, and with 20 time steps, is listed in Table III. As expected, for a low-light-yield scintillator such as BGO, the time required is lower than the time required for a high yield scintillator such as $\text{LaBr}_3:5\%\text{Ce}$.

V. CONCLUSION

We have developed a discrete-time discrete-event MC simulation framework to model the response of the SiPM to scintillation light. The model considers all the relevant processes that occur within a SiPM. The model response is compared with experimental data obtained from two Hamamatsu S10362-33-050C SiPMs coupled to $\text{LaBr}_3:5\%\text{Ce}$ crystals, and with some cases where the SiPM response is known *a priori*. The model is also used to study the effect of varying over-voltage and readout-circuit resistance on the SiPM response, perform sensitivity analysis, predict the SiPM response to different scintillators, and study the different SiPM phenomena individually. The MC model can also be used to determine the variance in the computed SiPM output. We have also shown that the model can help in determining difficult-to-measure SiPM parameters such as the detector PDE. Due to all these novel capabilities, the model provides us with a efficient tool

to analyze and simulate SiPM behavior comprehensively, and thus aid in the various tasks that require relating SiPM output to scintillation light.

We have also derived an analytic expression for the single-photoelectron response, and the current across the quenching resistance of the SiPM microcell. We have validated the expressions by comparing them with the output obtained using the LTSpice IV circuit-simulation software. These expressions are needed to accurately simulate the different phenomena in the SiPM and to understand the behavior of SiPMs. Also, the values of the current and voltage drop across the quenching resistance cannot even be measured experimentally [30]. Thus, the presence of an analytic expression for these quantities is useful. While a circuit-simulation software can be used to obtain these current and voltage drops, since these software are essentially discrete time, they can suffer from interpolation errors when required to find the output at a specific time. On the contrary, using the analytic expressions, we can compute the exact value of these voltage drops at any time value accurately. Apart from that, implementing an analytic expression in a simulation is often easier compared to the task of integrating a circuit-simulation software into another simulation. Moreover, the expressions are useful for studying the electrical characteristics and the pulse shapes of the SiPM. These, in turn, are necessary for their optimized use in different applications, in particular for the design of front-end electronics for SiPM-based detectors [31], [50]. Since the expressions are analytic, the optimization procedures can be implemented on numerical-computing software such as Matlab, instead of the current methods of using circuit-simulation software [31]. The presence of an analytic expression for an optimization task is advantageous, since different calculus-based methods can easily be applied on the analytic expressions. Finally, the analytic expression can also be used to simulate the transient response of the SiPM. This is especially useful in PET systems where the SiPM is used to gather timing information.

We will make the source code of our software available via the corresponding author to anyone interested. Thus, a SiPM end-user will be able to fine tune this code for their own specific application. Similarly, if a new advance is made in the field of SiPM science or technology, the scientist or designer will be able to modify our code to include the new development, and study the SiPM response. Finally, with regard to the process of generating scintillation light, we have kept our software package general. The software requires the time stamps of all the photons that are incident on the SiPM, and this list can be obtained using simulation-software like Geant [51], SCOUT [52] or any software that a system designer has designed for their system.

APPENDIX A SiPM CIRCUIT ANALYSIS

In this Appendix, we analyze the SiPM circuit and derive the expression for $I_0(t)$, as mentioned in (8). Consider the equivalent SiPM circuit shown in Fig. 2. Applying the Kirchhoff's voltage law across the different paths between $G_2 - G_1$, we obtain the following equations:

$$V_{\text{bias}} - V_d(t) - V_q(t) - V_s(t) = 0 \quad (21a)$$

$$V_{\text{bias}} - V_1(t) - V_2(t) - V_s(t) = 0 \quad (21b)$$

$$V_{\text{bias}} - V_g(t) - V_s(t) = 0. \quad (21c)$$

Using Kirchhoff's current law at nodes A, B and C, respectively, we obtain

$$I_d(t) + C_d \frac{dV_d(t)}{dt} + (N_{\text{cells}} - 1)C_d \frac{dV_1(t)}{dt} + C_g \frac{dV_g(t)}{dt} = \frac{V_s(t)}{R_s} \quad (22a)$$

$$I_d(t) + C_d \frac{dV_d(t)}{dt} = \frac{V_q(t)}{R_q} + C_q \frac{dV_q(t)}{dt} \quad (22b)$$

$$C_d \frac{dV_1(t)}{dt} = \frac{V_2(t)}{R_q} + C_q \frac{dV_2(t)}{dt}. \quad (22c)$$

Transforming (21a)–(22c) to Fourier domain, with the notation $\mathcal{F}\{V(t)\} = V(\omega)$ yields

$$V_{\text{bias}}\delta(\omega) - V_d(\omega) - V_s(\omega) = V_q(\omega) \quad (23a)$$

$$V_{\text{bias}}\delta(\omega) - V_1(\omega) - V_s(\omega) = V_2(\omega) \quad (23b)$$

$$V_{\text{bias}}\delta(\omega) - V_g(\omega) - V_s(\omega) = 0 \quad (23c)$$

$$I_d(\omega) + j\omega C_d V_d(\omega) + j\omega(N_{\text{cells}} - 1)C_d V_1(\omega) + j\omega C_g V_g(\omega) = \frac{V_s(\omega)}{R_s} \quad (23d)$$

$$I_d(\omega) + j\omega C_d V_d(\omega) = \frac{V_q(\omega)}{R_q} + j\omega C_q V_q(\omega) \quad (23e)$$

$$j\omega C_d V_1(\omega) = \frac{V_2(\omega)}{R_q} + j\omega C_q V_2(\omega). \quad (23f)$$

Substituting the expression for $V_2(\omega)$ from (23b) into (23f), and after some rearranging of terms, we obtain

$$\begin{aligned} & \left[j\omega(C_d + C_q) + \frac{1}{R_q} \right] V_1(\omega) \\ &= \left[\frac{1}{R_q} + j\omega C_q \right] [V_{\text{bias}}\delta(\omega) - V_s(\omega)]. \end{aligned} \quad (24)$$

Similarly, substituting the expression for $V_q(\omega)$ from (23a) into (23e) yields

$$\begin{aligned} I_d(\omega) + \left[j\omega(C_d + C_q) + \frac{1}{R_q} \right] V_d(\omega) \\ = \left[\frac{1}{R_q} + j\omega C_q \right] [V_{\text{bias}}\delta(\omega) - V_s(\omega)]. \end{aligned} \quad (25)$$

Using (23c), (24) and (25) in (23d), we solve for $V_s(\omega)$ in terms of $I_d(\omega)$, which yields

$$\begin{aligned} V_s(\omega) = & \frac{I_d(\omega)R_s(1 + j\omega\tau_2)}{1 + j\omega(\tau_1 + \tau_3 + \tau_4) - \omega^2(\tau_1\tau_4 + \tau_2\tau_3)} \\ & + V_{\text{bias}}\delta(\omega)j\omega \frac{\tau_3(1 + j\omega\tau_2) + \tau_4(1 + j\omega\tau_1)}{1 + j\omega(\tau_1 + \tau_3 + \tau_4) - \omega^2(\tau_1\tau_4 + \tau_2\tau_3)} \end{aligned} \quad (26)$$

where we have used (6a)–(6d) for ease of notation. We take the inverse Fourier transform on both sides of the above equation. Due to the sifting property of the $\delta(\omega)$ function, the terms involving V_{bias} disappear on performing the integration over ω . Therefore, we obtain

$$\begin{aligned} V_s(t) = & \frac{R_s}{2\pi} \int_{-\infty}^{\infty} d\omega \\ & \times \frac{I_d(\omega) \exp(j\omega t)(1 + j\omega\tau_2)}{(1 + j\omega(\tau_1 + \tau_3 + \tau_4) - \omega^2(\tau_1\tau_4 + \tau_2\tau_3))}. \end{aligned} \quad (27)$$

Finally, using Ohm's law, $I_s(t) = V_s(t)/R_s$, and thus the expression for $I_s(t)$ is obtained (8).

APPENDIX B CONTOUR INTEGRATION TO EVALUATE THE SINGLE- PHOTOELECTRON RESPONSE

In this Appendix, we solve the integral in (8) using contour integration. To evaluate the single-photoelectron response $I_s(t)$, we have to evaluate the expression given by (5), repeated here for convenience:

$$\begin{aligned} I_s(t) = & \frac{1}{2\pi} \int_{-\infty}^{\infty} d\omega \\ & \times \frac{I_d(\omega) \exp(j\omega t)(1 + j\omega\tau_2)}{1 + j\omega(\tau_1 + \tau_3 + \tau_4) - \omega^2(\tau_1\tau_4 + \tau_2\tau_3)} \end{aligned} \quad (28)$$

where $I_d(\omega)$ is the Fourier transform of the diode current. Since the denominator of the integrand in (28) is a quadratic expression, the roots of this expression are easily computed by evaluating the discriminant of the quadratic expression. Let us denote these roots by τ_{cd1} and τ_{cd2} . Then, using (7) to substitute

the expression for $I_d(\omega)$ in the above equation, we obtain the expression for $I_s(t)$ as

$$I_s(t) = \frac{Ge}{2\pi} \int_{-\infty}^{\infty} d\omega \times \frac{\exp(j\omega t)(1 + j\omega\tau_2)}{(1 + j\omega\tau_{cd1})(1 + j\omega\tau_{cd2})(1 + j\omega\tau_{mr})(1 + j\omega\tau_{md})}. \quad (29)$$

The above equation can further be rewritten as

$$I_s(t) = \frac{Ge}{2\pi\tau_{cd1}\tau_{cd2}\tau_{md}\tau_{mr}} \int_{-\infty}^{\infty} d\omega \times \frac{\exp(j\omega t)(1 + j\omega\tau_2)}{\left(\omega - \frac{j}{\tau_{cd1}}\right)\left(\omega - \frac{j}{\tau_{cd2}}\right)\left(\omega - \frac{j}{\tau_{md}}\right)\left(\omega - \frac{j}{\tau_{mr}}\right)}. \quad (30)$$

To solve this equation using contour-integration method, the variable ω is replaced by the complex variable z . We define the integrand to be the function $f(z)$ so that

$$f(z) = \frac{\exp(jzt)(1 + jz\tau_2)}{\left(z - \frac{j}{\tau_{cd1}}\right)\left(z - \frac{j}{\tau_{cd2}}\right)\left(z - \frac{j}{\tau_{md}}\right)\left(z - \frac{j}{\tau_{mr}}\right)}. \quad (31)$$

Our task then is to evaluate the integral

$$I_s(t) = \frac{Ge}{2\pi\tau_{cd1}\tau_{cd2}\tau_{md}\tau_{mr}} \int_{-\infty}^{\infty} f(z)dz. \quad (32)$$

As shown in Fig. 15, the poles of the integrand $f(z)$ lie on the imaginary axis in the upper half of the complex plane. Typically for a SiPM, $\tau_{cd1} > \tau_{cd2} > \tau_{md} > \tau_{mr}$. Since $t > 0$, to evaluate this integral using contour-integration, we consider a contour C in the upper half of the complex plane, as shown in Fig. 15 and evaluate $f(z)$ along this contour. This contour consists of two parts, C_1 and C_2 . While C_1 is along the real line from the complex point $(-R, 0)$ to the complex point $(R, 0)$, C_2 is along the upper half of a semicircle of radius R centered at the origin. To determine $I_s(t)$, we consider the case where $R \rightarrow \infty$. Using Jordan's lemma [53], we can show that as $R \rightarrow \infty$, the value of the integral over the contour C_2 is zero. Therefore

$$\int_C dz f(z) = \int_{C_1} dz \times \frac{\exp(jzt)(1 + jz\tau_2)}{\left(z - \frac{j}{\tau_{cd1}}\right)\left(z - \frac{j}{\tau_{cd2}}\right)\left(z - \frac{j}{\tau_{md}}\right)\left(z - \frac{j}{\tau_{mr}}\right)}. \quad (33)$$

The left hand side of the above equation, i.e., $\int_C dz f(z)$, is evaluated using the residue theorem. To illustrate briefly, the

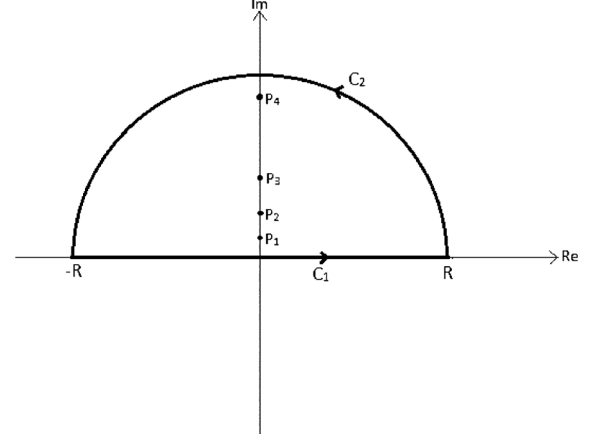


Fig. 15. The contour over which we perform the integration to evaluate $I_s(t)$.

poles of $f(z)$ are at j/τ_{cd1} , j/τ_{cd2} , j/τ_{md} and j/τ_{mr} . We therefore evaluate the residues at each of these poles. For example, the residue at $z = (j)/(\tau_{cd1})$ is given by

$$\begin{aligned} Res_{z=\frac{j}{\tau_{cd1}}} &= \lim_{z \rightarrow \frac{j}{\tau_{cd1}}} \left(z - \frac{j}{\tau_{cd1}}\right) f(z) \\ &= \frac{j \exp\left(-\frac{t}{\tau_{cd1}}\right) \left(1 - \frac{\tau_2}{\tau_{cd1}}\right)}{\left(\frac{1}{\tau_{cd1}} - \frac{1}{\tau_{cd2}}\right) \left(\frac{1}{\tau_{cd1}} - \frac{1}{\tau_{md}}\right) \left(\frac{1}{\tau_{cd1}} - \frac{1}{\tau_{mr}}\right)}. \end{aligned} \quad (34)$$

Using the residue theorem [53]

$$\begin{aligned} \int_C f(z)dz &= 2\pi j \left[Res_{z=\frac{j}{\tau_{cd1}}} f(z) + Res_{z=\frac{j}{\tau_{cd2}}} f(z) \right. \\ &\quad \left. + Res_{z=\frac{j}{\tau_{md}}} f(z) + Res_{z=\frac{j}{\tau_{mr}}} f(z) \right], \end{aligned} \quad (35)$$

From (29)–(35), we obtain the expression for $I_s(t)$ (8).

APPENDIX C

CURRENT ACROSS QUENCHING RESISTOR

In this Appendix, we obtain the expression for the current across the quenching resistance due a single avalanche, given by (11). Using the expression for $V_d(\omega)$ from (25) in (23a), we obtain the expression for $V_q(\omega)$ as

$$\begin{aligned} V_q(\omega) &= \frac{I_d(\omega)R_q}{1 + j\omega\tau_1} - V_s(\omega) \frac{j\omega R_q C_d}{1 + j\omega\tau_1} \\ &\quad + V_{bias} \delta(\omega) \frac{j\omega R_q C_d}{1 + j\omega\tau_1}. \end{aligned} \quad (36)$$

$$\begin{aligned} I_q(t) &= \frac{Ge}{2\pi} \int d\omega \frac{\exp(j\omega t)}{(1 + j\omega\tau_1)(1 + j\omega\tau_{md})(1 + j\omega\tau_{mr})} \\ &\quad - \frac{R_s Ge}{2\pi} \int d\omega \\ &\quad \times \frac{j\omega R_q C_d (1 + j\omega\tau_2) \exp(j\omega t)}{(1 + j\omega\tau_1)(1 + j\omega\tau_{md})(1 + j\omega\tau_{mr})(1 + j\omega\tau_{cd1})(1 + j\omega\tau_{cd2})} \end{aligned} \quad (38)$$

Substituting the expression for $V_s(\omega)$ from (26) into the above equation and performing an inverse Fourier transform, we obtain

$$V_q(t) = R_q \int d\omega \frac{I_d(\omega) \exp(j\omega t)}{1 + j\omega\tau_1} - R_s \times \int d\omega \frac{I_d(\omega)(1 + j\omega\tau_2)j\omega R_q C_d \exp(j\omega t)}{[1 + j\omega\tau_1][1 + j\omega(\tau_1 + \tau_3 + \tau_4) - \omega^2(\tau_1\tau_4 + \tau_2\tau_3)]} \quad (37)$$

where the terms containing V_{bias} disappear on invoking the the shifting property of the δ function. The denominator in the above integrand has the same quadratic expression as the integrand in (28). Therefore, we replace the quadratic expression by the $(1 + j\omega\tau_{cd1})(1 + j\omega\tau_{cd2})$. Also replacing the expression for $I_d(\omega)$ from (7) in (37), and using Ohm's law to determine $I_q(t)$ yields (38), shown at the bottom of the previous page, which is solved using contour integration. The derivation is similar to the derivation in Appendix B. This yields the expression for $I_q(t)$, given by (11).

ACKNOWLEDGMENT

The authors would like to thank Dr. Harrison H. Barrett, Dr. Masud Mansuripur, Vaibhav Bora, Robin Palit and Stefan Seifert for helpful discussions, and Dr. Lars Furenlid for reviewing an earlier draft of the manuscript.

REFERENCES

- [1] G. Bondarenko *et al.*, "Limited geiger-mode microcell silicon photodiode: New results," *Nucl. Instrum. Meth. Phys. Res. A*, vol. 442, no. 1–3, pp. 187–192, 2000.
- [2] V. Golovin and V. Saveliev, "Novel type of avalanche photodetector with geiger mode operation," *Nucl. Instrum. Meth. Phys. Res. A*, vol. 518, no. 1–2, pp. 560–564, 2004, frontier Detectors for Frontier Physics: Proceedings.
- [3] M. Ghioni, A. Gulinatti, I. Rech, F. Zappa, and S. Cova, "Progress in silicon single-photon avalanche diodes," *IEEE J. Sel. Top. Quant. Electron.*, vol. 13, no. 4, pp. 852–862, Jul.–Aug. 2007.
- [4] P. Buzhan *et al.*, "An advanced study of silicon photomultiplier," ICFA Instrum. Bulletin 2001.
- [5] C. Niclass, M. Sergio, and E. Charbon, "A single photon avalanche diode array fabricated in 0.35 μm CMOS and based on an event-driven readout for TCSPC experiments," *SPIE*, vol. 6372, 2006.
- [6] C. Piemontesi *et al.*, "Recent developments on silicon photomultipliers produced at FBK-irst," in *Proc. IEEE Nucl. Sci. Symp. Conf. Rec.*, Nov. 2007, vol. 3, pp. 2089–2092.
- [7] M. Mazzillo *et al.*, "Timing performances of large area silicon photomultipliers fabricated at STMicroelectronics," *IEEE Trans. Nucl. Sci.*, vol. 57, no. 4, pp. 2273–2279, Aug. 2010.
- [8] E. Grigoriev *et al.*, "Silicon photomultipliers and their bio-medical applications," *Nucl. Instrum. Meth. Phys. Res. A*, vol. 571, no. 1–2, pp. 130–133, 2007.
- [9] S. Cova, A. Longoni, and A. Andreoni, "Towards picosecond resolution with single-photon avalanche diodes," *Rev. Sci. Instrum.*, vol. 52, no. 3, pp. 408–412, 1981.
- [10] S. Moehrs, A. Del Guerra, D. J. Herbert, and M. A. Mandelkern, "A detector head design for small-animal PET with silicon photomultipliers (SiPM)," *Phys. Med. Biol.*, vol. 51, no. 5, p. 1113, 2006.
- [11] S. Yamamoto *et al.*, "Development of a Si-PM-based high-resolution PET system for small animals," *Phys. Med. Biol.*, vol. 55, no. 19, p. 5817, 2010.
- [12] S. I. Kwon *et al.*, "Development of small-animal PET prototype using silicon photomultiplier (SiPM): Initial results of phantom and animal imaging studies," *J. Nucl. Med.*, vol. 52, pp. 572–579, Apr. 2011.
- [13] G. Llosa *et al.*, "Novel silicon photomultipliers for PET applications," *IEEE Trans. Nucl. Sci.*, vol. 55, no. 3, pp. 877–881, Jun. 2008.
- [14] S. Espana *et al.*, "Performance evaluation of SiPM detectors for PET imaging in the presence of magnetic fields," in *Proc. IEEE Nucl. Sci. Symp. Conf. Rec.*, Oct. 2008, pp. 3591–3595.
- [15] D. R. Schaart *et al.*, "SiPM-array based PET detectors with depth-of-interaction correction," in *Proc. IEEE Nucl. Sci. Symp. Conf. Rec.*, Oct. 2008, pp. 3581–3585.
- [16] A. Nassalski *et al.*, "Silicon photomultiplier as an alternative for APD in PET/MRI applications," in *Proc. IEEE Nucl. Sci. Symp. Conf. Rec.*, Oct. 2008, pp. 1620–1625.
- [17] S. Yamamoto *et al.*, "Interference between PET and MRI sub-systems in a silicon-photomultiplier-based PET/MRI system," *Phys. Med. Biol.*, vol. 56, no. 13, p. 4147, 2011.
- [18] M. T. Madsen, "Recent advances in SPECT imaging," *J. Nucl. Med.*, vol. 48, no. 4, pp. 661–672, 2007.
- [19] D. Renker, "New developments on photosensors for particle physics," *Nucl. Instrum. Meth. Phys. Res. A*, vol. 598, no. 1, pp. 207–212, 2009.
- [20] V. Andreev *et al.*, "A high-granularity scintillator calorimeter readout with silicon photomultipliers," *Nucl. Instrum. Meth. Phys. Res. A*, vol. 540, no. 2–3, pp. 368–380, 2005.
- [21] F. Retiere *et al.*, "Characterization of multi pixel photon counters for T2K near detector," *Nucl. Instrum. Meth. Phys. Res. A*, vol. 610, no. 1, pp. 378–380, 2009.
- [22] F. Retiere, "MPPC response simulation and high speed readout optimization," in *Proc. IEEE Nucl. Sci. Symp. Conf. Rec.*, Nov. 2009, pp. 2197–2200.
- [23] M. Grodzicka, M. Moszynski, T. Szczesniak, M. Kapusta, M. Szawlowski, and D. Wolski, "Energy resolution of scintillation detectors with SiPM light readout," in *Proc. IEEE Nucl. Sci. Symp. Conf. Rec.*, Nov. 2010, pp. 1940–1948.
- [24] H. T. van Dam *et al.*, "A comprehensive model of the response of silicon photomultipliers," *IEEE Trans. Nucl. Sci.*, vol. 57, no. 4, pp. 2254–2266, Aug. 2010.
- [25] V. C. Spanoudaki and C. S. Levin, "Scintillation induced response in passively-quenched Si-based single photon counting avalanche diode arrays," *Opt. Exp.*, vol. 19, no. 2, pp. 1665–1679, Jan. 2011.
- [26] P. Eckert, H.-C. Schultz-Coulon, W. Shen, R. Stamen, and A. Tadday, "Characterisation studies of silicon photomultipliers," *Nucl. Instrum. Meth. Phys. Res. A*, vol. 620, no. 2–3, p. 11, 2010.
- [27] H. Barrett, W. Hunter, B. Miller, S. Moore, Y. Chen, and L. Furenlid, "Maximum-likelihood methods for processing signals from gamma-ray detectors," *IEEE Trans. Nucl. Sci.*, vol. 56, no. 3, pp. 725–735, Jun. 2009.
- [28] F. Zappa, A. Tosi, A. D. Mora, and S. Tisa, "SPICE modeling of single photon avalanche diodes," *Sens. Actuators A, Phys.*, vol. 153, no. 2, pp. 197–204, 2009.
- [29] P. J. Hambleton, S. A. Plimmer, J. P. R. David, and G. J. Rees, "Simulated current response in avalanche photodiodes," *J. Appl. Opt.*, vol. 91, pp. 2107–2111, 2002.
- [30] S. Seifert *et al.*, "Simulation of silicon photomultiplier signals," *IEEE Trans. Nucl. Sci.*, vol. 56, no. 6, pp. 3726–3733, Dec. 2009.
- [31] F. Corsi *et al.*, "Modelling a silicon photomultiplier (SiPM) as a signal source for optimum front-end design," *Nucl. Instrum. Meth. Phys. Res. A*, vol. 572, no. 1, pp. 416–418, 2007.
- [32] S. S. Majos, P. Achenbach, and J. Pochodzalla, "Characterisation of radiation damage in silicon photomultipliers with a Monte Carlo model," *Nucl. Instrum. Meth. Phys. Res. A*, vol. 594, no. 3, pp. 351–357, 2008.
- [33] D. Henseler, R. Grazioso, N. Zhang, and M. Schmand, "SiPM performance in PET applications: An experimental and theoretical analysis," in *Proc. IEEE Nucl. Sci. Symp. Conf. Rec.*, Nov. 2009, pp. 1941–1948.
- [34] J. Pulko, F. R. Schneider, A. Velroyen, D. Renker, and S. I. Ziegler, "A Monte-Carlo model of a SiPM coupled to a scintillating crystal," *J. Instrum.*, vol. 7, no. 02, p. P02009, 2012.
- [35] M. Haigh, A. Vacheret, F. Retiere, T. Lindner, and S. Oser, "Monte Carlo simulation of MPPC photosensors for the T2K experiment," in *Proc. Int. Workshop on New Photon Detectors, Shinshu, Japan, PoS(PD09)*, 2009, p. 007.
- [36] J.-H. Cha and M.-I. Roh, "Combined discrete event and discrete time simulation framework and its application to the block erection process in shipbuilding," *Adv. Eng. Softw.*, vol. 41, no. 4, pp. 656–665, 2010.
- [37] D. van Beek, J. Rooda, and M. van den Muyzenberg, A. Javor, A. Lehmann, and I. Molnar, Eds., "Specification of combined continuous-time/discrete-event models," in *Proc. European Simulation Multiconf.*, 1996, pp. 219–224.
- [38] W.-S. Choong, "The timing resolution of scintillation-detector systems: Monte Carlo analysis," *Phys. Med. Biol.*, vol. 54, no. 21, pp. 6495–6513, 2009.

- [39] D. Orme, T. Nakaya, M. Yokoyama, and A. Minamino, "Measurement of PDE of MPPC with different wavelengths of light," presented at the PD09, PoS (PD09), 2009, vol. 19.
- [40] S. Cova, M. Ghioni, A. Lacaita, C. Samori, and F. Zappa, "Avalanche photodiodes and quenching circuits for single-photon detection," *Appl. Opt.*, vol. 35, no. 12, pp. 1956–1976, Apr. 1996.
- [41] N. Pavlov, G. Mashlum, and D. Meier, "Gamma spectroscopy using a silicon photomultiplier and a scintillator," in *Proc. IEEE Nucl. Sci. Symp. Conf. Rec.*, Oct. 2005, vol. 1, pp. 173–180.
- [42] S. Cova, A. Lacaita, and G. Ripamonti, "Trapping phenomena in avalanche photodiodes on nanosecond scale," *IEEE Electron Device Lett.*, vol. 12, no. 12, pp. 685–687, Dec. 1991.
- [43] Y. Du and F. Reti, "After-pulsing and cross-talk in multi-pixel photon counters," *Nucl. Instrum. Meth. Phys. Res. A*, vol. 596, no. 3, pp. 396–401, 2008.
- [44] Y. Kang, H. X. Lu, Y.-H. Lo, D. S. Bethune, and W. P. Risk, "Dark count probability and quantum efficiency of avalanche photodiodes for single-photon detection," *App. Phys. Lett.*, vol. 83, no. 14, pp. 2955–2957, Oct. 2003.
- [45] T. Frach, G. Prescher, C. Degenhardt, R. de Gruyter, A. Schmitz, and R. Ballizany, "The digital silicon photomultiplier; Principle of operation and intrinsic detector performance," in *Proc. IEEE Nucl. Sci. Symp. Conf. Rec.*, Nov. 2009, pp. 1959–1965.
- [46] M. Engelhardt, "LTSpice IV," Linear Technology Corporation, Sept. 2011, version 4.12r [Online]. Available: <http://www.linear.com/designtools/software/#LTSpice>
- [47] A. Stoykov, Y. Musienko, A. Kuznetsov, S. Reucroft, and J. Swain, "On the limited amplitude resolution of multipixel Geiger-mode APD," *J. Instrum.*, vol. 2, no. 06, p. P06005, 2007.
- [48] J. de Haas and P. Dorenbos, "Advances in yield calibration of scintillators," *IEEE Trans. Nucl. Sci.*, vol. 55, no. 3, pp. 1086–1092, Jun. 2008.
- [49] "Saint-Gobain material product sheets for LaBr3:Ce, NaI:Tl, BGO, and LYSO," Saint-Gobain. Hiram, OH.
- [50] A. Para, P. Rubinov, and I. Vasilas, "Pulse shape and other electrical characteristics of silicon photomultipliers," presented at the IEEE Nucl. Sci. Symp. Med. Imag. Conf., 2011.
- [51] S. Agostinelli *et al.*, "Geant4—A simulation toolkit," *Nucl. Instrum. Meth. Phys. Res. A*, vol. 506, no. 3, pp. 250–303, 2003.
- [52] W. Hunter *et al.*, "SCOUT: A fast Monte-Carlo modeling tool of scintillation camera output," in *Proc. IEEE Nucl. Sci. Symp. Conf. Rec.*, Nov. 6 2010, pp. 1203–1208.
- [53] G. B. Arfken and H. H. Weber, *Mathematical Methods for Physicists*, 6th ed. New York: Elsevier, 2005.